Events Meet Phase-Shifting Digital Holography: Practical Acquisition, Theory, and Algorithms

Ittetsu Uchiyama¹, Chihiro Tsutake^{1*}, Keita Takahashi¹, and Toshiaki Fujii¹

Department of Information and Communication Engineering, Nagoya University, Furo-cho, Chikusa-ku, Nagoya, 464-8603, Japan

Abstract

We introduce a novel phase-shifting digital holography (PSDH) method leveraging a hybrid event-based vision sensor (EVS). The key idea of our method is the phase shift during a single exposure. The hybrid EVS records a hologram blurred by the phase shift, together with the events corresponding to blur variations. We present analytical and optimization-based methods that theoretically support the reconstruction of full-complex wavefronts from the blurred hologram and events. The experimental results demonstrate that our method achieves a reconstruction quality comparable to that of a conventional PSDH method while enhancing the acquisition efficiency.

1 Introduction

Wavefront reconstruction is a fundamental problem in optics that has attracted significant attention across diverse applications [1]. In light of the physical limitations of sensors, various optical and computational methods [2–5] have been developed to reconstruct complex wavefronts from constrained data. Among these, we focus on digital holography [2], which captures intensity frames as holograms via an interferometric measurement. Due to the large pixel size of sensors, interference fringe spacing should be as large as possible to avoid aliasing noise. While in-line holography has the capability of maximizing the fringe spacing, it suffers from zero-order and twin images [6] in the reconstructed wavefronts.

Phase-shifting digital holography (PSDH) [7] is one of the methods for eliminating the unwanted images. Figure 1 shows a schematic illustration of PSDH. A phase shifter modulates the global phase of the reference beam and an image sensor records a hologram, which is the intensity of interference fringes formed between the reference and object beams. Figure 2a shows a timing chart of acquisition. In PSDH, recording a hologram for each shifting value is essential, but it is highly time-consuming. Parallel digital holography [8, 9] can resolve this temporal issue by spatially multiplexing holograms in a single frame. However, the parallel methods sacrifice the spatial resolution of holograms, thereby degrading the quality of the reconstructed wavefronts.

 $^{^*}$ ctsutake@nagoya-u.jp

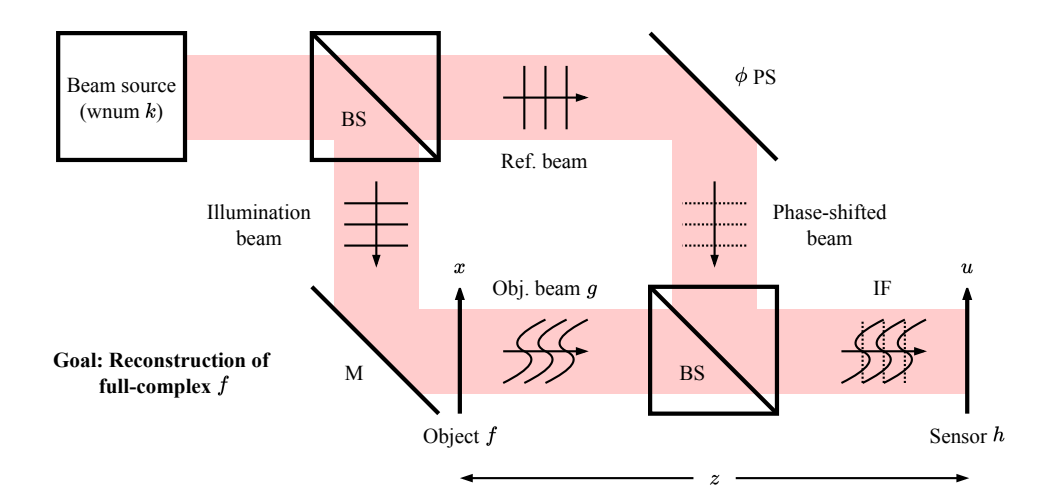


Figure 1: Phase-shifting digital holography (PSDH). Red region: optical path. BS: beam splitter. M: mirror. PS: phase shifter. IF: interference fringe. k: wavenumber. ϕ : phase-shifting value. Conventional method: ordinary image sensor. Our method: hybrid event-based vision sensor (EVS).

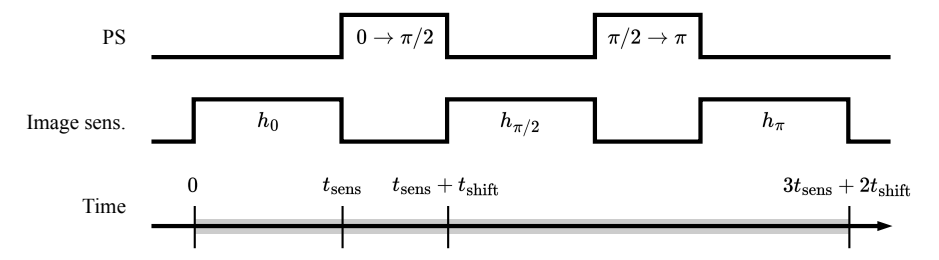
To address the temporal issue without sacrificing the spatial resolution, we introduce a novel PSDH method leveraging a hybrid event-based vision sensor (EVS) [10], which can record absolute intensity frames and relative intensity changes, i.e., events, in a logarithmic scale. The key idea of our method is the phase shift of the reference beam during a single exposure¹, as illustrated in Fig. 2b. The hybrid EVS records a hologram blurred by the phase shift, together with the events corresponding to blur variations. We present a closed-form representation of the object wavefront in a noiseless setup, which can be computed from the blurred hologram and events. We also propose an optimization-based method to stabilize the wavefront reconstruction. The experimental results demonstrate that our method achieves a reconstruction quality comparable to that of a conventional PSDH method while enhancing the acquisition efficiency.

2 Preliminaries

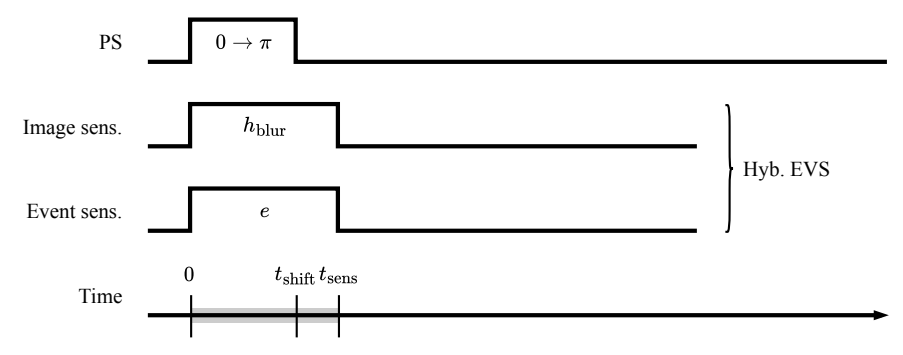
Terminologies. The conventional PSDH [7] that only uses frames (non-blurred holograms) is referred to as F-PSDH. The proposed method that incorporates a single frame (blurred hologram) and events is referred to as FE-PSDH.

Optics. As shown in Fig. 1, without loss of generality, we consider one-dimensional object and sensor planes. The complex wavefront on the object plane is denoted by f. The intensity distribution on the sensor plane, i.e., the hologram, is denoted by h. We assume that f and h are parallel and located at a distance z from each other. The coordinates on the object and sensor planes are denoted by x and u, respectively. For notational simplicity, we sometimes omit the coordinates when they can be inferred from the context. The complex wavefront of the object beam is denoted by g. As shown in Fig. 2, we assume that F-PSDH and FE-PSDH share the same exposure time for capturing a single frame, which is denoted by $t_{\rm sens}$. The operating time of a phase shifter is denoted

¹A similar idea was effective for light field imaging with a coded aperture [11].



(a) Conventional frame-only PSDH (F-PSDH) with image sensor. Three exposures with discrete phase shifts of $0 \to \pi/2$ and $\pi/2 \to \pi$.



(b) Proposed frame-and-event PSDH (FE-PSDH) with hybrid EVS. Single exposure with continuous phase shift of $0 \to \pi$.

Figure 2: Timing charts of acquisition. $t_{\rm sens}$: exposure time of sensor. $t_{\rm shift}$: transient time of phase shifter. Gray bar: total acquisition time. Phase-shifting value is initialized to 0 before the first exposure. Throughout this paper, we assume $t_{\rm shift} \leq t_{\rm sens}$ and both methods share $t_{\rm sens}$ and $t_{\rm shift}$. Acquisition time of conventional method: $3t_{\rm sens} + 2t_{\rm shift}$. Our method: $t_{\rm sens}$ —single exposure time alone.

by t_{shift} . We assume $t_{\text{shift}} \leq t_{\text{sens}}$. The wavenumber of a beam is denoted by k. The phase-shifting value is denoted by ϕ . We set $\phi = 0$ before acquisition.

Mathematics. The imaginary unit is denoted by j. The amplitude of a real or complex number is denoted by $|\cdot|$. The complex conjugate is denoted by $\bar{\cdot}$. The Euclidean norm of a function is denoted by $|\cdot|_2$.

3 Principle of F-PSDH

In this section, we mention a general method for reconstructing the object wavefront f from the intensity frames obtained by an ordinary image sensor. The complex wavefront of the object beam at the sensor plane, i.e., g, is represented as the wave propagated from f based on the Fresnel diffraction integral [12]. Let r be the complex wavefront of the reference beam at the sensor plane. As shown in Fig. 1, a phase shifter modulates the global phase of r, resulting in $r \exp(j\phi)$. A digital hologram, i.e., the intensity of interference fringes formed between g and $r \exp(j\phi)$, can be

formulated as

$$h_{\phi} = |g + r \exp(j\phi)|^2 = |g|^2 + |r|^2 + \bar{g}r \exp(j\phi) + g\bar{r} \exp(-j\phi).$$
 (1)

The terms $|g|^2 + |r|^2$ and $\bar{g}r \exp(j\phi)$ are referred to as the zero-order and twin images, respectively. To eliminate these unwanted images, the three-step method [7] is used here, which records h_0 , $h_{\pi/2}$, h_{π} with three exposures. By combining the three holograms, the complex wavefront g can be perfectly reconstructed as

$$g = \frac{1-j}{4\bar{r}} \left(h_0 - h_{\pi/2} + j(h_{\pi/2} - h_{\pi}) \right). \tag{2}$$

The complex object wavefront f can be obtained from g and the reverse Fresnel diffraction integral. In conventional F-PSDH, alternating the phase shift and frame recording is essential, which increases acquisition time. Specifically, if the operations of a phase shifter and an image sensor are synchronized, the three-step method requires $3t_{\rm sens} + 2t_{\rm shift}$, as shown in Fig. 2a.

4 Proposed method: FE-PSDH

4.1 Data acquisition

To efficiently acquire data for reconstructing f within a practical time, we replace the conventional image sensor with the hybrid EVS [10]. It is an extension of the image sensor, in which each pixel has a standard photon-detecting element with a bio-inspired event-sensing circuit. This design allows the EVS to simultaneously capture absolute light intensity and detect changes in log light intensity. As illustrated in Fig. 2b, we parallelize the phase shift with the frame and event recording, where the phase of the reference beam is modulated from 0 to π during a single exposure. With this design, the EVS records a hologram blurred by the phase shift, which is denoted by $h_{\rm blur}$. At the same time, the events triggered by blur variations are obtained asynchronously, which are denoted by e. Notably, as shown in Fig. 2b, the acquisition time can be reduced to $t_{\rm sens}$, the single exposure time.

4.2 Analytical reconstruction in noiseless setup

In this sub-section, we prove that f can be recovered from the ideal noiseless h_{blur} and e. Before deriving a reconstruction method, we define mathematical models of the frame and event recording.

Frame recording model. Let t=0 be the beginning time of exposure and the synchronized phase shift, $T_{\text{frame}} = [0, t_{\text{sens}}]$ be a continuous time duration for frame exposure, and $\phi(t)$ be the phase-shifting value during its transition at time $t \in T_{\text{frame}}$. The noiseless frame h_{blur} can be modeled as the integration of non-blurred holograms in (1) over t as follows:

$$h_{\text{blur}} = \int_{T_{\text{frame}}} h_{\phi(t)} dt = \lim_{M \to \infty} \frac{1}{M} \sum_{m=1}^{M} h_{\phi(t_{\text{sens}} m/M)}, \tag{3}$$

where $h_{\phi(t)}$ represents the hologram at the phase-shifting value $\phi = \phi(t)$.

Event recording model. During the exposure, the EVS records the discrete time, spatial coordinate, and polarity of intensity changes. Let $T_{\text{event}} \subseteq T_{\text{frame}}$ be a set of recorded discrete times during the exposure. Events can be viewed as a set of signed delta functions, as

$$e(t,u) = \pm \delta \Big(u - u(t) \Big), \tag{4}$$

where u(t) is the spatial coordinate of the event recorded at the time $t \in T_{\text{event}}$. An event is triggered when the intensity change exceeds a contrast threshold [10], denoted by C, i.e.,

$$\left| \log \left(h_{\phi(t)}(u) \right) - \log \left(h_{\phi(t_{\text{prev}})}(u) \right) \right| > C, \tag{5}$$

where t_{prev} is the time when the previous event was recorded. We accumulate events from t=0 to a prescribed time t for each u as follows:

$$E_{0 \to \phi(t)}(u) = \sum_{\tau} e(\tau, u) \quad \text{s.t.} \quad \tau \in T_{\text{event}} \quad \text{and} \quad \tau \le t.$$
 (6)

Equations (5) and (6) lead to the following approximate relationship;

$$E_{0 \to \phi(t)} = \frac{1}{C} \Big(\log h_{\phi(t)} - \log h_0 \Big), \tag{7}$$

where $h_0 = h_{\phi(0)}$ and $\phi(0) = 0$.

We define \mathcal{E} as the integration of $E_{0\to\phi(t)}$ over the continuous time $t\in T_{\text{frame}}$ as follows:

$$\mathcal{E} = \int_{T_{\text{frame}}} \exp\left(CE_{0\to\phi(t)}\right) dt = \lim_{N\to\infty} \frac{1}{N} \sum_{n=1}^{N} \exp\left(CE_{0\to\phi(t_{\text{sens}}n/N)}\right). \tag{8}$$

By transforming (7), we can obtain

$$h_{\phi(t)} = h_0 \exp\left(CE_{0\to\phi(t)}\right). \tag{9}$$

Combining (3), (8), and (9), we have

$$h_{\text{blur}} = \int_{T_{\text{frame}}} h_0 \exp\left(CE_{0 \to \phi(t)}\right) dt = \mathcal{E}h_0, \quad \therefore h_0(u) = \frac{h_{\text{blur}}(u)}{\mathcal{E}(u)}. \tag{10}$$

From (2), (7), and (10), the object wavefront at the hologram plane, i.e., g, can be reconstructed as follows:

$$g = \frac{1-j}{4\bar{r}} \cdot h_0 \left\{ 1 - \frac{h_{\pi/2}}{h_0} + j \left(\frac{h_{\pi/2}}{h_0} - \frac{h_{\pi}}{h_0} \right) \right\}$$
 (11)

$$= \frac{1-j}{4\bar{r}} \cdot \frac{h_{\text{blur}}}{\mathcal{E}} \left\{ 1 - \exp(CE_{0\to\pi/2}) + j \left(\exp(CE_{0\to\pi/2}) - \exp(CE_{0\to\pi}) \right) \right\}. \tag{12}$$

Note that the right-hand side can be computed from the noiseless $h_{\rm blur}$ and e. We can obtain the full-complex wavefront at the object plane, i.e., f, from g and the reverse Fresnel diffraction integral, as was done in F-PSDH.

4.3 Reconstruction by optimization

To compute $E_{0\to\pi/2}$ in (12), it is essential to determine a time when $\phi(t)=\pi/2$, hereafter denoted by $t_{\pi/2}$. In the noiseless setup, this task is straightforward because $t_{\pi/2}$ can be computed from the response characteristic of the phase shifter. In the practical noisy case, h_{blur} and e are affected by various sources of noise, such as pixel-wise fluctuations of the contrast threshold [13]. For such noisy data, we find that the exact $t_{\pi/2}$ value does not always present the best reconstruction, as will be demonstrated in Section 5.1. Taking this background into account, we introduce an optimization-based reconstruction method that stably presents the accurate wavefront reconstruction in noisy conditions. In the following, the noisy versions of h_{blur} and e are denoted by h_{blur} and e, respectively.

We first formulate an optimization problem to jointly recover h_0 and the time $t_{\pi/2}$. Let us define the object wavefront at the sensor plane, parameterized by variables $h_{0,\text{opt}}$ (real function) and $t_{\pi/2,\text{opt}}$ (real number), as follows:

$$\tilde{g}\left(h_{0,\text{opt}}, t_{\pi/2,\text{opt}}\right) = \frac{1-j}{4\bar{r}} \cdot h_{0,\text{opt}} \left\{ 1 - \exp\left(C\tilde{E}_{0\to\phi(t_{\pi/2,\text{opt}})}\right) + j\left(\exp\left(C\tilde{E}_{0\to\phi(t_{\pi/2,\text{opt}})}\right) - \exp\left(C\tilde{E}_{0\to\pi}\right)\right) \right\}, \quad (13)$$

where $\tilde{E}_{0\to\phi(t_{\pi/2,\mathrm{opt}})}$ and $\tilde{E}_{0\to\pi}$ are computed by replacing e in (6) with \tilde{e} . We define the following two loss functions based on (1) and (10):

$$L_1(h_{0,\text{opt}}, t_{\pi/2,\text{opt}}) = \left\| h_{0,\text{opt}} - \left| \tilde{g}(h_{0,\text{opt}}, t_{\pi/2,\text{opt}}) + r \right|^2 \right\|_2^2, \tag{14}$$

$$L_2(h_{0,\text{opt}}) = \|\tilde{\mathcal{E}}h_{0,\text{opt}} - \tilde{h}_{\text{blur}}\|_2^2, \tag{15}$$

where $\tilde{\mathcal{E}}$ is computed by replacing $E_{0\to\phi(t)}$ in (8) with $\tilde{E}_{0\to\phi(t)}$. We formulate the optimization problem of the form

$$\min_{h_{0,\text{opt}}, t_{\pi/2,\text{opt}}} L(h_{0,\text{opt}}, t_{\pi/2,\text{opt}}) = L_1(h_{0,\text{opt}}, t_{\pi/2,\text{opt}}) + \lambda L_2(h_{0,\text{opt}}),$$
(16)

where λ is a positive hyperparameter.

We then solve the above problem using gradient descent, as

$$h_{0,\text{opt}}[i+1] = h_{0,\text{opt}}[i] - \alpha_h \nabla L \Big(h_{0,\text{opt}}[i], t_{\pi/2,\text{opt}}[i] \Big),$$
 (17)

$$t_{\pi/2,\text{opt}}[i+1] = t_{\pi/2,\text{opt}}[i] - \alpha_t \frac{\partial}{\partial t_{\pi/2,\text{opt}}} L\Big(h_{0,\text{opt}}[i], t_{\pi/2,\text{opt}}[i]\Big), \tag{18}$$

where ∇ is the gradient operator with respect to $h_{0,\mathrm{opt}}, i$ is the number of the current iteration, $h_{0,\mathrm{opt}}[i]$ and $t_{\pi/2,\mathrm{opt}}[i]$ are the variables at i, and α_h and α_t are learning rates. The gradient descent updates are repeated until the index i reaches the predefined maximum number of iterations I. Let \tilde{f} denote the complex object wavefront reconstructed from noisy data. In the optimization-based method, we obtain \tilde{f} from $g = \tilde{g} \left(h_{0,\mathrm{opt}}[I], t_{\pi/2,\mathrm{opt}}[I] \right)$ and the reverse Fresnel diffraction integral.

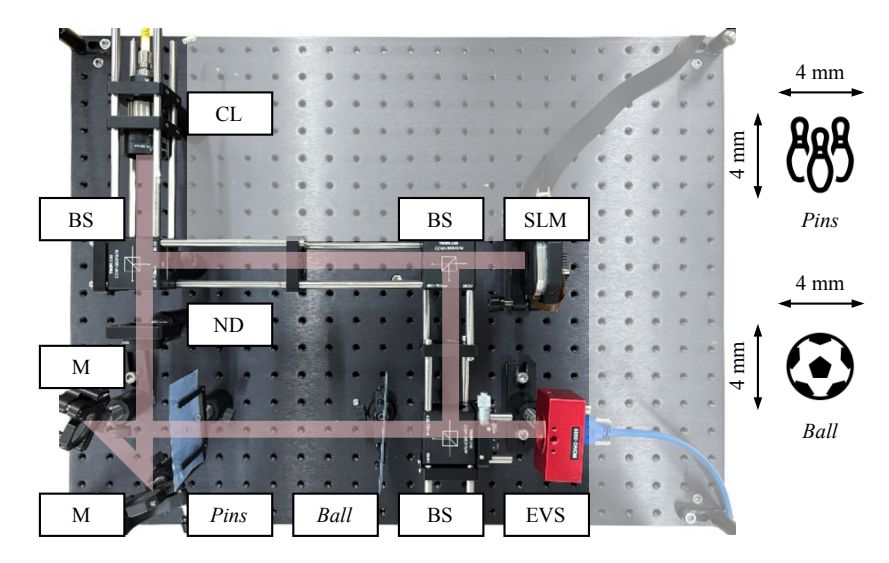


Figure 3: Optical implementation of acquisition system in Fig. 1. CL: collimator lens. SLM: spatial light modulator. ND: neutral-density filter. *Ball* and *Pins* are printed on OHP sheets. EVS–*Ball*: 120 mm. EVS–*Pins*: 270 mm.

Table 1: Specifications of phase shifter (SLM-210) and hybrid EVS (DAVIS346).

Model	#pixels	Pixel size [µm]	Time [s]
Santec SLM-210	1920×1200	8.0×8.0	$t_{\rm shift} = 1/60$
iniVation DAVIS346	346×260	18.5×18.5	$t_{ m sens}=1/25$

4.4 Implementation details

Optics. Figure 3 illustrates an optical implementation of the acquisition system in Fig. 1. The beam source was Thorlabs KLS635 of the wavelength 635 nm; thus, the wavenumber was $k = 2\pi/635$ rad/nm. The collimator lens converts the incident beam into the front-parallel beam; thus, the amplitude of r was constant. Santec SLM-210, a reflection-type spatial light modulator (SLM), serves as a phase shifter, which can modulate the phase of the incident reference beam pixel by pixel. We placed an iniVation DAVIS346, a hybrid EVS, at the sensor plane, which has the capability of recording monochrome frames and events. The specifications of the phase shifter and hybrid EVS are summarized in Table 1. To reconstruct the full-complex wavefronts of three-dimensional objects, the pins and ball patterns were printed on OHP sheets and placed at distances of z = 270 mm and 120 mm from the EVS, respectively. The sizes of the printed objects were about 4×4 mm.

Algorithms. We present pseudo codes of the analytical reconstruction method (Section 4.2) and optimization-based method (Section 4.3) in Algorithms 1 and 2, respectively. In Algorithm 1, we used noisy $\tilde{h}_{\rm blur}$ and \tilde{e} instead of noiseless $h_{\rm blur}$ and e. We estimated the oracle value $t_{\pi/2}$ and used the resulting value, denoted by $t_{\pi/2,\rm anal}$, as $t_{\pi/2}$. In Algorithm 2, we implemented the gradient descent (18) leveraging the autograd functionality [14] in PyTorch. During the forward pass (lines 5 and 6), non-differentiable operations were detached from the computational graph. The initial values $h_{0,\rm opt}[0]$ and $t_{\pi/2,\rm opt}[0]$ were sampled from the normal distribution $\mathcal{N}(0,1)$ and

Algorithm 1 Analytical reconstruction for noisy data

```
Input: \tilde{h}_{\text{blur}} (noisy hologram), \tilde{e} (noisy events), and t_{\pi/2,\text{anal}} (hyperparameter).

1: Compute \tilde{E}_{0\to\pi/2} and \tilde{E}_{0\to\pi}.

2: Compute \tilde{\mathcal{E}}.

3: Compute \tilde{g}.

4: Compute \tilde{f}.

b Use (noisy events), and t_{\pi/2,\text{anal}} (hyperparameter).

b Use (noisy hologram), \tilde{e} (noisy events), and t_{\pi/2,\text{anal}} (hyperparameter).

b Use \tilde{E}_{0\to\pi/2}, t = t_{\text{sens}} for \tilde{E}_{0\to\pi}, and t = \tilde{e}.

c Use (noisy hologram), \tilde{e} (noisy events), and t_{\pi/2,\text{anal}} for \tilde{E}_{0\to\pi/2}, t = t_{\text{sens}} for \tilde{E}_{0\to\pi}, and t = \tilde{e}.

b Use (noisy hologram), \tilde{e} (noisy events), and t_{\pi/2,\text{anal}} for \tilde{E}_{0\to\pi/2}, t = t_{\text{sens}} for \tilde{E}_{0\to\pi}, and t = \tilde{e}.

b Use (noisy hologram), \tilde{e} (noisy events), and t_{\pi/2,\text{anal}} for \tilde{E}_{0\to\pi/2}, t = t_{\text{sens}} for \tilde{E}_{0\to\pi}, and t = \tilde{e}.

c Use (noisy hologram), \tilde{E}_{0\to\pi/2} and \tilde{E}_{0\to\pi/2}, t = t_{\text{sens}} for \tilde{E}_{0\to\pi}, and t = \tilde{e}.

c Use (noisy hologram), \tilde{E}_{0\to\pi/2} and t = \tilde{e}.

c Use (noisy hologram), \tilde{E}_{0\to\pi/2} and t = \tilde{e}.
```

Algorithm 2 Optimization-based reconstruction using autograd in PyTorch

```
Input: h_{\text{blur}}, \tilde{e}, and \lambda (hyperparameter).
 1: Compute \tilde{\mathcal{E}}.
                                                                                                                                                                       \triangleright Use (8) and e = \tilde{e}.
 2: Compute \tilde{E}_{0\to\pi}.
                                                                                                                                                     \triangleright Use (6), t = t_{\text{sens}}, and e = \tilde{e}.
 3: Initialize h_{0,\text{opt}}[0] and t_{\pi/2,\text{opt}}[0].
                                                                                                                                         \triangleright Drawn from \mathcal{N}(0,1) and \mathcal{U}(0,t_{\text{sens}}).
 4: for i = 0 to I do
            Compute \tilde{E}_{0 \to \phi(t_{\pi/2, \text{opt}}[i])}.
                                                                                                                                            \triangleright Use (6), t = t_{\pi/2, \text{opt}}[i], and e = \tilde{e}.
 5:
                                                                                                            \triangleright Use (15), h_{0,\text{opt}} = h_{0,\text{opt}}[i], and t_{\pi/2,\text{opt}} = t_{\pi/2,\text{opt}}[i].
 6:
            Compute L(h_{0,\text{opt}}[i], t_{\pi/2,\text{opt}}[i]).
            Compute h_{0,\text{opt}}[i+1] and t_{\pi/2,\text{opt}}[i+1] via backpropagation.
                                                                                                                                                                      \triangleright Equivalent to (18).
 8: end for
 9: Compute f.
                                                                                           \triangleright Use reverse Fresnel diffraction and g = \tilde{g}(h_{0,\text{opt}}[I], t_{\pi/2,\text{opt}}[I]).
```

the uniform distribution $\mathcal{U}(0, t_{\text{sens}})$, respectively (line 3). We used the learning rates $\alpha_h = 0.005$ and $\alpha_t = 0.0005$. The maximum number of iterations I was 2500. In both Algorithms 1 and 2, we set N = 64 and C = 0.15.

5 Experiment

5.1 Stability analysis

To verify the stability of Algorithms 1 and 2 with respect to hyperparameter selection, we evaluate their performance through computer simulations.

Dataset of object wavefront. We sampled 200 images of size 346×260 from the CLIC2020 dataset [15]. The images were monochrome and had luminance values ranging from 0 to 1. The pixel pitch was 18.5×18.5 µm. We generated 100 complex object wavefronts f, where half of the sampled images were used as the intensity of f. The remaining 100 images were assigned as phase data, with the luminance values scaled by a factor of 2π . We placed f at z = 120 mm.

Dataset of blurred hologram and event. We simulated 100 noiseless blurred holograms $h_{\rm blur}$ from the above-mentioned object wavefronts, using M=500 and the front-parallel r with a constant intensity of 0.5. We implemented the Fresnel diffraction integral using the band-limited angular spectrum method [16]. The pixel pitch of the holograms was 18.5×18.5 µm. We computed noisy holograms $\tilde{h}_{\rm blur}$ by adding zero-mean Gaussian noise and applying 8-bit quantization to $h_{\rm blur}$; the noise standard deviation $\sigma_{\rm frame}$ was set to 0, 0.01, or 0.02. Following [13], we assumed that the contrast threshold fluctuates pixel by pixel. In the event generation process, we used Gaussian noise of mean 0.15 and standard deviation $\sigma_{\rm event}=0.015$ as pixel-wise contrast thresholds. When

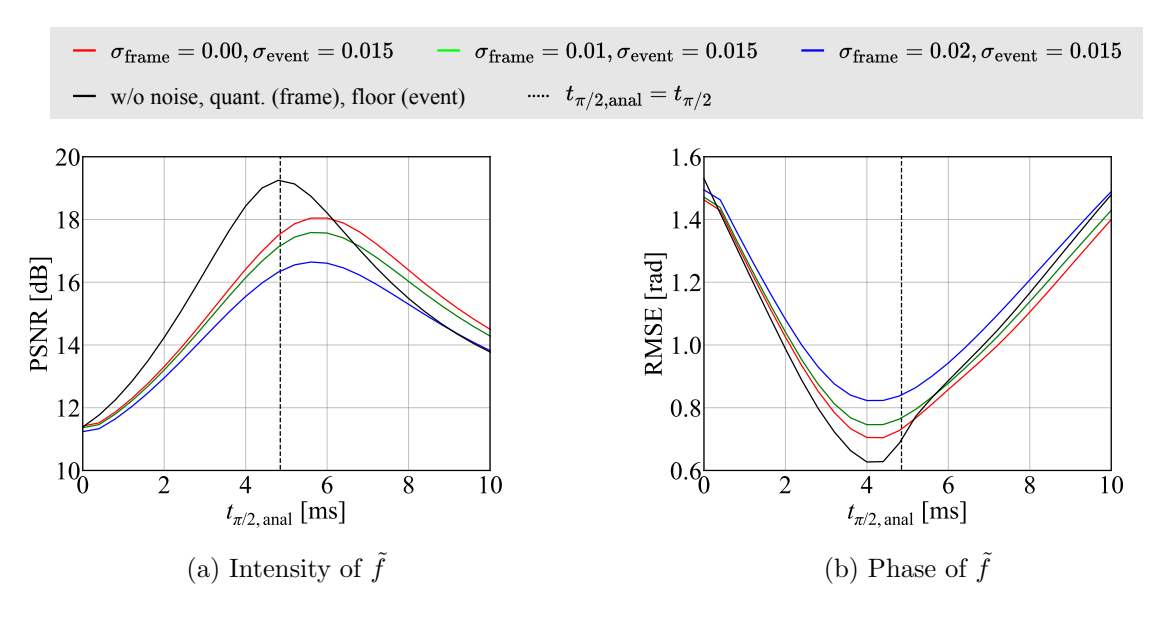


Figure 4: Errors by Algorithm 1 against $t_{\pi/2,\text{anal}}$.

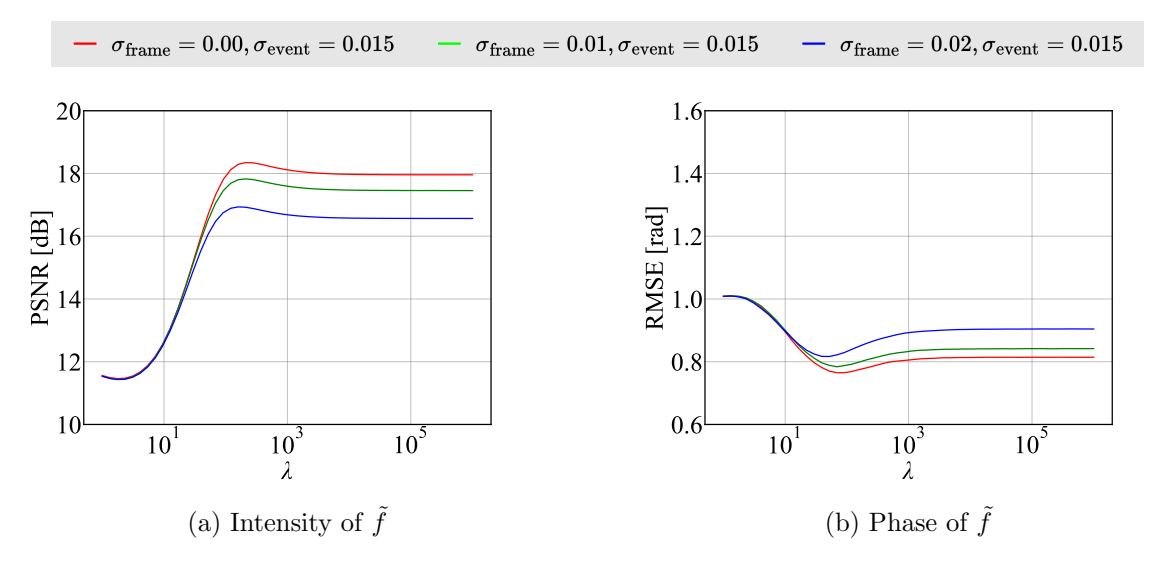


Figure 5: Errors by Algorithm 2 against λ .

computing (7), we applied the floor operation to its right-hand side.

Response characteristic of SLM. Following [17], we modeled the phase transition from 0 to π as the following non-linear time-evolution function:

$$\phi(t) = \pi \left(1 - \exp(-t/t_{\text{speed}}) \right), \tag{19}$$

where $t_{\rm speed}$ controls the transition speed and was set to 7 ms. Note that $t_{\pi/2}$ was 4.85 ms.

Evaluation metrics. We measured peak signal-to-noise ratio (PSNR) values [dB] between the

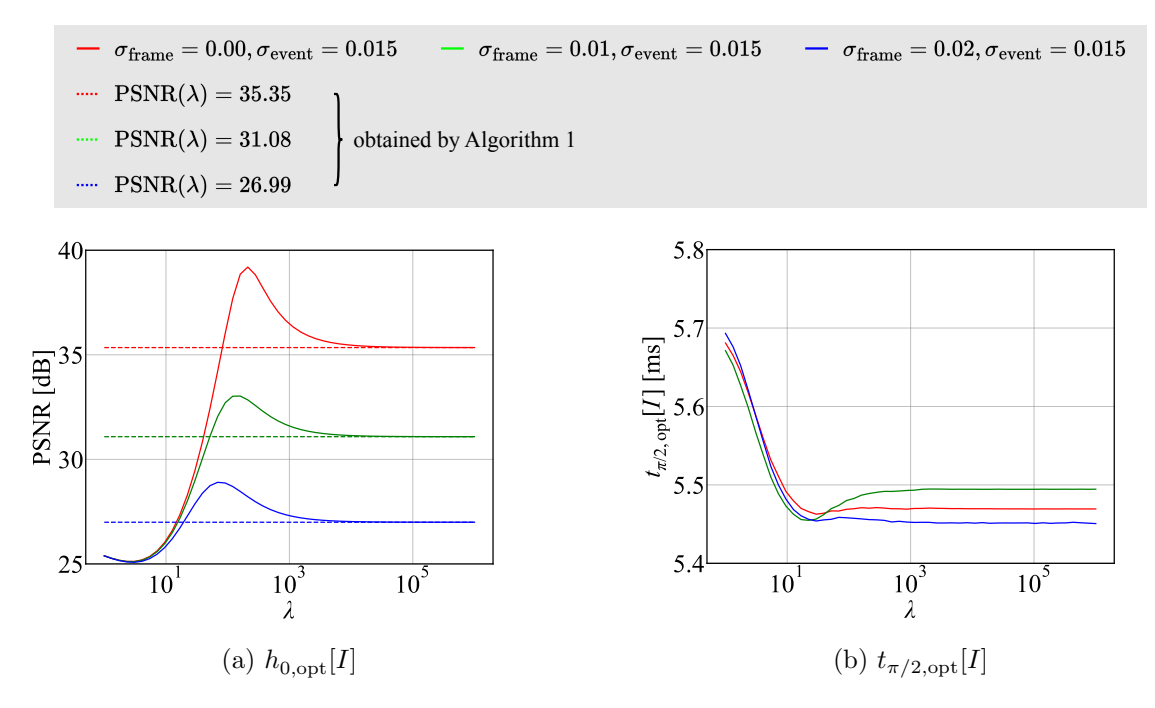


Figure 6: PSNR of $h_{0,\text{opt}}[I]$ and reconstructed time $t_{\pi/2,\text{opt}}[I]$.

intensities of f and \tilde{f} . The quality of the reconstructed phases was evaluated using root-mean-squared error (RMSE) [rad] values, where the phases corresponding to zero intensities were removed from the computation.

Results on Algorithm 1. Figure 4 shows the PSNR and RMSE values as functions of $t_{\pi/2,\rm anal}$. In the noiseless scenario (black lines), the maximum and minimum values in 4a and 4b, respectively, appeared near $t_{\pi/2,\rm anal} = t_{\pi/2}$. However, in the noisy counterpart (colored lines), PSNR and RMSE values were optimized at $t_{\pi/2,\rm anal}$ that is apart from $t_{\pi/2}$. Moreover, even a small deviation from the optimal $t_{\pi/2,\rm anal}$ value resulted in a sharp decline in the reconstruction quality. These characteristics make the analytical method difficult to use for noisy real-world data as the determination of the optimal $t_{\pi/2,\rm anal}$ is non-trivial.

Remark 1. For the red, green, and blue lines in Fig. 4, PSNR values between ideal h_0 and \tilde{h}_0 , i.e., $\tilde{h}_{\text{blur}}/\tilde{\mathcal{E}}$, were 35.35, 31.08, and 26.99 dBs, respectively.

Results on Algorithm 2. Next, we demonstrate the stability of Algorithm 2 by changing λ . Figures 5a and 5b summarize the results. When $100 \le \lambda$, Algorithm 2 consistently achieved nearly optimal reconstruction. This result indicates that, unlike Algorithm 1, Algorithm 2 is largely insensitive to the choice of hyperparameter. Moreover, Algorithm 2 stably presents reasonable reconstruction quality by choosing a large λ .

Remark 2. Figure 6a shows PSNR values between h_0 and reconstructed $h_{0,\text{opt}}[I]$, which were higher than those of Algorithm 1. Figure 6b indicates $t_{\pi/2,\text{opt}}[I]$, which were slightly larger than

²The errors cannot be reduced to zero due to the band-limitation of the Fresnel diffraction integral.

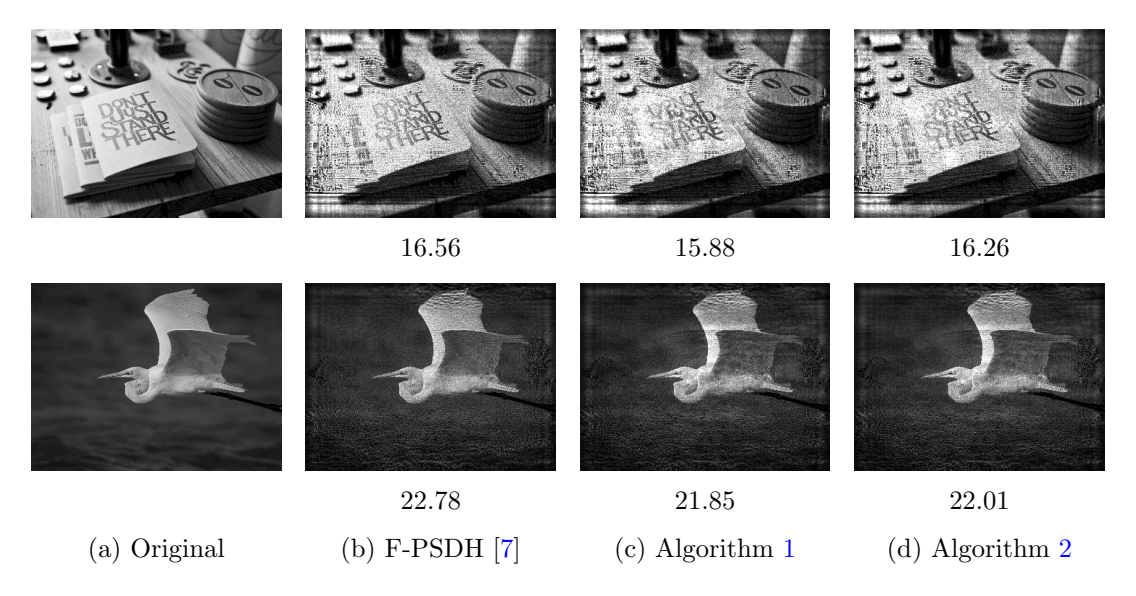


Figure 7: Reconstructed intensities with PSNRs [dB] in simulation. $\sigma_{\rm frame} = 0.01$, $\sigma_{\rm event} = 0.015$, $t_{\pi/2,\rm anal} = 4.85$ ms in Algorithm 1, and $\lambda = 500$ in Algorithm 2.

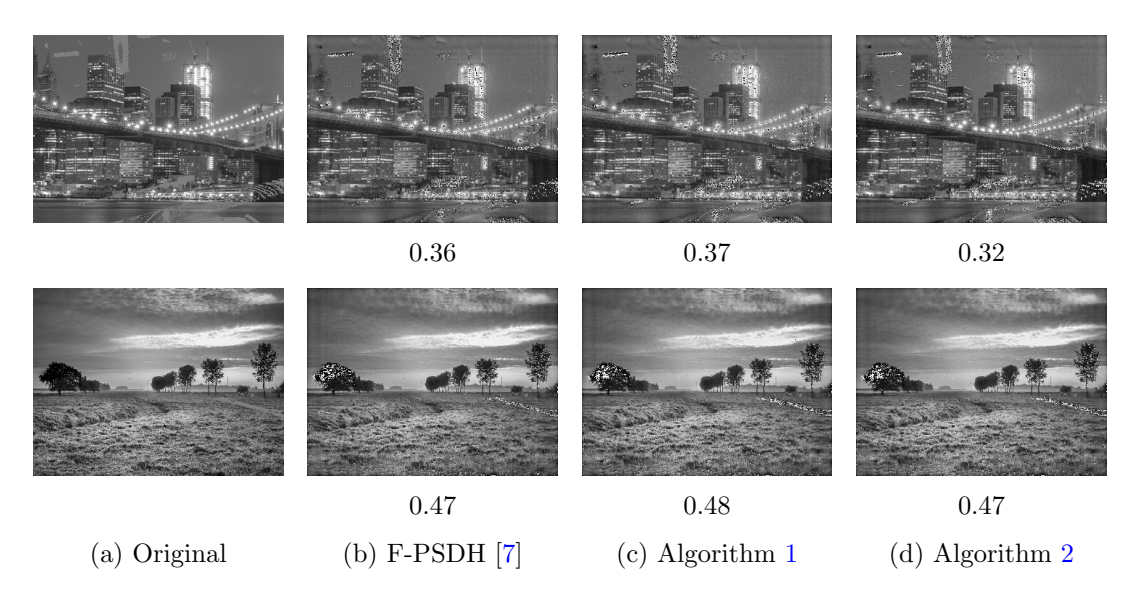


Figure 8: Reconstructed phases with RMSEs [rad] in simulation. We used same parameters as in Fig. 7.

 $t_{\pi/2}$, similar to Fig. 4a.

5.2 Comparison with F-PSDH

To demonstrate the effectiveness of FE-PSDH, we visualize the reconstructed wavefronts and compare them with those obtained by F-PSDH. The experiments were conducted both on computer

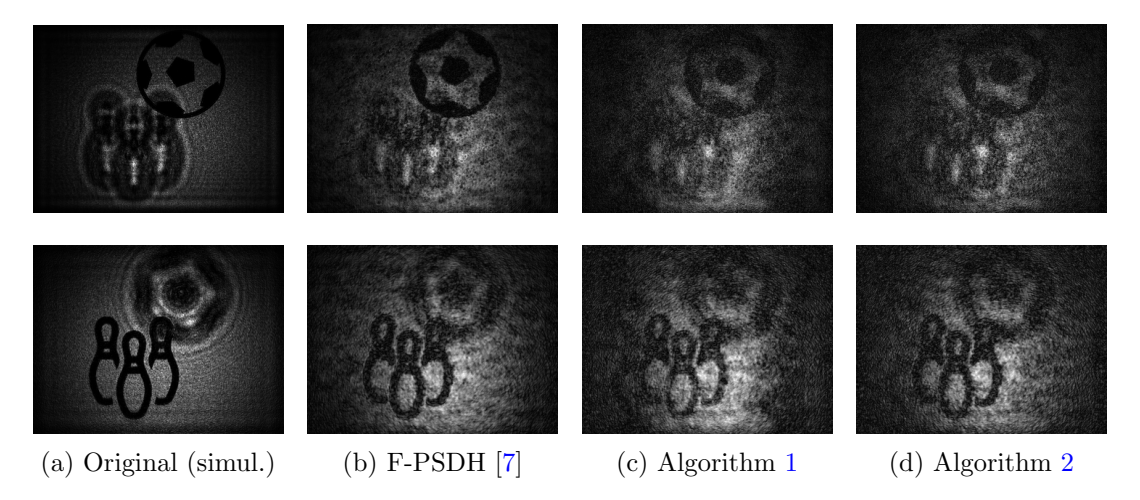


Figure 9: Reconstructed intensities using real-world data recorded by optical system in Fig. 3. Top: front focus (z = 120 mm). Bottom: back focus (z = 270 mm).

simulations and the optical system in Fig. 3.

Configuration of F-PSDH. For the simulation, we generated the noiseless h_0 , $h_{\pi/2}$, and h_{π} by varying ϕ in (1), where the intensity and phase of f were produced in the same manner as in Section 5.1. We added Gaussian noise of variance $\sigma_{\text{frame}} = 0.01$ and applied 8-bit quantization to the generated holograms. For the optical experiment, we recorded the holograms by the image sensor in the hybrid EVS, DAVIS346, through the three exposures and two phase shifts. The object wavefronts were reconstructed by (2) and the reverse Fresnel diffraction, where noisy holograms were used as h_0 , $h_{\pi/2}$, and h_{π} .

Results on simulation. Figure 7 presents the reconstructed intensities and Fig. 8 shows their corresponding phases. Algorithm 1 produced noisy results due to the misalignment of the empirical $t_{\pi/2,\text{anal}}$ value and the optimal one. In contrast, Algorithm 2 exhibited results comparable to those by F-PSDH.

Results on optical experiment. Figure 9 illustrates the reconstructed intensities using the real data, where all the methods can successfully reproduce the bokeh effect. Similar to Fig. 7, F-PSDH and Algorithm 2 presented fine details of the *ball* and *pins* at z=120 and 270 mm, respectively. We believe the qualities of the reconstructed wavefronts were nearly equivalent.

These results demonstrate that FE-PSDH, particularly, Algorithm 2, can stably and reliably reconstruct object wavefronts while accelerating the acquisition time.

6 Conclusion

Inspired by F-PSDH, we introduced a novel wavefront reconstruction pipeline using the hybrid EVS. The data for reconstructing wavefonts can be measured within the single exposure time alone, which is the remarkable characteristic of our method. We demonstrated the robustness of

our method via simulation and optical experiments. We believe our approach will potentially offer a new perspective on holography.

References

- [1] S. Gigan *et al.*, "Roadmap on wavefront shaping and deep imaging in complex media," *Journal of Physics: Photonics*, vol. 4, no. 4, p. 042501, 2022.
- [2] J. Goodman and R. W. Lawrence, "Digital image formation from electronically detected holograms," *Applied Physics Letters*, vol. 11, no. 3, pp. 77–79, 1967.
- [3] J. R. Fienup, "Phase retrieval algorithms: a comparison," *Applied Optics*, vol. 21, no. 15, pp. 2758–2769, 1982.
- [4] N. Streibl, "Phase imaging by the transport equation of intensity," *Optics Communications*, vol. 49, no. 1, pp. 6–10, 1984.
- [5] B. C. Platt and R. Shack, "History and principles of Shack-Hartmann wavefront sensing," *Journal of Refractive Surgery*, vol. 17, no. 5, pp. S573–S577, 2001.
- [6] E. Stoykova, H. Kang, and J. Park, "Twin-image problem in digital holography—a survey," *Chinese Optics Letters*, vol. 12, no. 6, p. 060013, 2014.
- [7] I. Yamaguchi and T. Zhang, "Phase-shifting digital holography," Optics Express, vol. 22, no. 16, pp. 1268–1270, 1997.
- [8] Y. Awatsuji, M. Sasada, and T. Kubota, "Parallel quasi-phase-shifting digital holography," *Applied Physics Letters*, vol. 85, no. 6, pp. 1069–1071, 2004.
- [9] T. Tahara *et al.*, "Experimental demonstration of parallel two-step phase-shifting digital holography," *Optics Express*, vol. 18, no. 18, pp. 18 975–18 980, 2010.
- [10] P. Lichtsteiner, C. Posch, and T. Delbruck, "A 128 × 128 120 dB 15 µs latency asynchronous temporal contrast vision sensor," *IEEE Journal of Solid-State Circuits*, vol. 43, no. 2, pp. 566–576, 2008.
- [11] S. Habuchi, K. Takahashi, C. Tsutake, T. Fujii, and H. Nagahara, "Time-efficient light-field acquisition using coded aperture and events," in *Proceedings of the IEEE/CVF Conference on Computer Vision and Pattern Recognition*, 2024, pp. 24923–24933.
- [12] J. W. Goodman, Introduction to Fourier Optics. Roberts & Co. Publishers, 2005.
- [13] Y. Hu, S. C. Liu, and T. Delbruck, "v2e: From video frames to realistic DVS events," in Proceedings of IEEE/CVF Conference on Computer Vision and Pattern Recognition Workshops, 2021.
- [14] A. G. Baydin, B. A. Pearlmutter, A. A. Radul, and J. M. Siskind, "Automatic differentiation in machine learning: A survey," *Journal of Machine Learning Research*, vol. 18, no. 1, pp. 5595–5637, 2017.

- [15] https://archive.compression.cc.
- [16] K. Matsushima and T. Shimobaba, "Band-limited angular spectrum method for numerical simulation of free-space propagation in far and near fields," *Optics Express*, vol. 17, no. 22, pp. 19662–19673, 2009.
- [17] G. Thalhammer, R. W. Bowman, G. D. Love, M. J. Padgett, and M. R.-Marte, "Speeding up liquid crystal SLMs using overdrive with phase change reduction," *Journal of Machine Learning Research*, vol. 21, no. 2, pp. 1779–1797, 2013.